Gravity Waves Enhance the Extreme Precipitation in Henan, China, July 2021

Xiang Feng[1], Feimin Zhang[1], and Chenghai Wang[1]

[1] Key Laboratory of Arid Climate Resource and Environment of Gansu Province (ACRE)，College of Atmospheric Sciences, Lanzhou University, Lanzhou, China.

Corresponding author: Chenghai Wang (wch@lzu.edu.cn)

Key Points:

- The gravity waves associated with banded convection southwest of the rainfall center enhance extreme precipitation.
- The gravity waves originated from a mountain and propagated through a stable wave duct at altitude of 5 to 9 km.
- The downward wave energy from these gravity waves interact with the upward wave energy from gravity waves excited by latent heating.

Abstract

This study utilizes radar, sounding observations, and convective-permitting simulations with a non-hydrostatic mesoscale model to investigate the effects of gravity waves originating from the southwest mountain on the intensification of the extreme precipitation event occurred in Henan Province, Central China, in July 2021 (referred to as the "21.7" event). The gravity waves have wave speeds of approximately 11.5 m s^{-1} and wavelengths ranging from 60 to 90 km. These gravity waves are generated by the interaction between a northwest-southeast direction mountain (Funiu Mountain, FNM) and a southwesterly flow originated from the mesoscale convective vortex (MCV) developing from an inverted trough southwest of the rainfall center. Then, these waves propagate northeastward through a wave duct featuring a stable layer between 5 and 9 km altitude, capped by a low-stability reflecting layer with a critical level. As they propagate, these waves trigger banded convective cells along their path. Upon the arrival of gravity wave peaks at the rainfall center, they induce the downward energy flux of gravity waves from high troposphere levels (~7 km). The downward wave energy dynamically interacts with the upward wave energy from gravity waves excited by latent heating at the lower tropospheric level (~1 km). This synergistic effect intensifies the ascending motion and results in a precipitation increase of over 20% at the rainfall center. This study highlights the significance of orographic gravity waves in shaping extreme precipitation events.

Plain Language Summary

On July 20, 2021, the city of Zhengzhou, China, experienced an unprecedented and exceptionally intense rainfall event, setting a new record for mainland China. The presence of banded convection suggests that gravity waves likely played a significant role in contributing to this extreme rainfall. These gravity waves originate from a mountain and propagate horizontally towards the rainfall center in the plain area on the leeward slope. Upon the arrival of the gravity wave at the rainfall center, the downward wave energy interacts with the upward wave energy from gravity waves excited by latent heating, resulting in the intensification of low-level upward motion and convection. In essence, this process underscores the notable role played by orographic gravity waves in amplifying extreme precipitation events.

1 Introduction

Heavy rainfall is one of a frequently occurred extreme weather phenomena that contributes significantly to urban waterlogging, floods, and debris flows (Tao, 1980). They are often generated by mesoscale convective systems (MCS), particularly quasi-stationary convective systems (QSCS), that exhibit a tendency to produce extremely large precipitation over a small area (Ding et al., 1978; Schumacher & Johnson, 2005; Schumacher, 2009; Schumacher & Rasmussen, 2020; Bai et al., 2021; Fu et al., 2022; Wei et al., 2023). The behavior of MCS, including their triggering, maintenance, and enhancement can be related to gravity waves (Zhang et al., 2001; Garvert et al., 2007; Wu et al., 2016; Hua et al., 2020).

In July 2021, an extreme heavy precipitation event occurred in Henan Province, central China, resulted in significant casualties and property damage (Su et al., 2021). Notably, on July 20, the Zhengzhou National Meteorological Observation Station recorded record-breaking hourly rainfall of 201.9 mm, surpassing previous records in mainland China (Su et al., 2021). Studies consensus attributed this exceptional rainfall to a QSCS above the rainfall center (Ran et al., 2021; Chyi et al., 2022; Wei et al., 2023). The formation and sustenance of this QSCS were influenced by multiple mesoscale systems, including the southwest airflow generated by the Mesoscale Convective Vortex (MCV) located west of the rainfall center (Fu et al., 2022), the expansive southeast low-level jet (Luo & Du, 2022), the mesoscale northeast barrier jet developed by the eastern slopes of the Taihang Mountain obstructing the easterly flow (Wei et al., 2023), and the northerly downslope gravity current caused by nocturnal radiative cooling on the southern slopes of the Taihang Mountain (Sun et al., 2023). Both the low-level jet and barrier jet are linked to terrain-blocking effects, while the south-west flow in front of the MCV may be influenced by terrain as it passes through the FNM. Thus, these converging airflows from various mesoscale systems were key contributors to the formation of QSCS.

To enhance the comprehension of the mechanisms underpinning the extreme rainfall event, extensive analysis has been carried out on the relationship between the QSCS evolution and convective cells southwest of the rainfall center. Ran et al. (2021) suggested that on July 20, a stable mesoscale cloud cluster was observed over the rainfall center, with small cloud clusters to continuously converging from the southwest, subsequently reinforcing the stable mesoscale cloud cluster. This stable mesoscale cloud cluster corresponded to the QSCS, while the small cloud clusters are associated with convective cells originating from the southwest (Ran et al., 221; Liang et al., 2022; Huang et al., 2022). Through radar reflectivity analysis, it has been revealed that these convective cells initiate at the Funiu mountain (FNM) and progress northeastward towards the rainfall center, resulting in the generation of southwest-northeast-oriented banded convection between the terrain and the center of rainfall. The merging of these convective cells with the QSCS leads to enhanced convection and extreme precipitation (Liang et al., 2022; Huang et al., 2022; Chyi et al., 2022; Wei et al., 2023). These results have consistently implied that orographic effects of FNM could be important for precipitation intensity. However, the mechanisms of orographic effects behind the extreme precipitation remain not clear, especially for their impacts on the formation and development of these convective cells.

Several studies have highlighted three key characteristics of the convective cells southwest of the rainfall center (Liang et al., 2022; Huang et al., 2022; Chyi et al., 2022; Wei et al., 2023). Firstly, during their propagation, these convective cells give rise to a band of convection oriented southwest-northeast. Secondly, the convective cells originate from the FNM. Thirdly, once these convective cells reach the rainfall center, the QSCS was significantly amplified (Ran et al., 2021; Huang, 2022; Wei et al., 2023). Band-like convective activities are commonly influenced by gravity waves (Lindzen & Tung, 1976; Zhang et al., 2001; Kirshbaum et al., 2007a; Kingsmill et al., 2016; Du & Zhang, 2019; Bai et al., 2021). Gravity waves can be excited by terrain (Scorer, 1949), and the vertical disturbances induced by gravity waves have the potential to trigger convection (Hua et al., 2020) and enhance precipitation (Wu et al., 2016). It is, therefore, plausible to assume that the convective cells southwest of the rainfall center are associated with gravity waves generated by the FNM. As these convective cells approach the rainfall center, the QSCS and precipitation may intensify due to the vertical disturbances induced by gravity waves.

The aforementioned studies provided evidence indicating the potential significant role of gravity waves in the "21.7" heavy rainfall event. The issue we concerned is: how do gravity waves contribute to precipitation in the center of "21.7" heavy rainfall? To address this issue, sensitivity simulations shall be conducted to examine the characteristics of convective cells southwest of the rainfall center, explore their potential correlation with gravity waves, and investigate the effects of gravity waves on precipitation during the "21.7" event.

The rest of this paper is arranged as follows: section 2 introduces data, methods, experiment design. Section 3 provides a brief overview of the "21.7" event, and validates the simulation results. In section 4, the relationship between convective cells (manifested as band convection) located southwest of the rainfall center and gravity waves， the mechanisms of gravity wave excitation and propagation , and the impact and mechanism of gravity waves on extreme precipitation will be investigated. Conclusion is summarized in section 5.

2 Data, methods and experiment design

2.1. Data

Composite radar reflectivity mosaics are used to analyze the spatiotemporal variations of convective cells. The fifth generation ECMWF (European Centre for Medium-Range Weather Forecasts) atmospheric reanalysis (ERA5) data (Hersbach et al., 2020) is used to drive WRF model. The *in-situ* soundings and synoptic surface observation are assimilated to improve the initial conditions. To analyze the rainfall, the hourly precipitation data from automatic stations, and the gridded hourly precipitation dataset form the CMA Land Data Assimilation System (CLDAS-V2.0) (Sun et al., 2020) were utilized. The above rainfall data, radar observations, and surface station data were obtained from the China Meteorological Data Service Center (CMDC).

2.2. Methods

To diagnose the excitation of gravity wave, the moist Brunt-Väisälä frequency was used to assess the hydrostatic stability of the analyzed moist air. For unsaturated air, it is defined as:

$$N_m^2 = g\frac{dln\theta_v}{dz} \tag{1}$$

where $\theta_v = \theta(1 + 0.608q)$ is virtual potential temperature, and q is the water vapor mixing ratio. For saturated moist air, based on the work of Durran and Klemp (1982), it is defined as:

$$N_m^2 = g\left\{\frac{1+(Lq_s/RT)}{1+(\epsilon L^2 q_s/c_p RT^2)} \times \left(\frac{dln\theta_v}{dz}\frac{L}{c_p T}\frac{dq_s}{dz}\right) - \frac{dq_w}{dz}\right\} \tag{2}$$

where T and θ are the sensible and potential temperatures of the atmosphere, g is gravitational acceleration, L is latent heat of vaporization, q_s is the saturation mixing ratio, q_w is the total water mixing ratio, R is the ideal gas constant for dry air, R_v is the gas constant for water vapor, $\epsilon = \frac{R}{R_v}$, c_p is the heat capacities of dry air. The square of the Scorer parameter l^2 defined as follows:

$$l^2 \approx \frac{N_m^2}{(\overline{u}-c)^2} - \frac{U_{zz}}{(\overline{u}-c)} \tag{3}$$

where N_m^2 is the saturated Brunt-Väisälä frequency squared, U_{zz} is the second derivative of $\overline{u}$, and c is the gravity wave phase speed (Yang and Houze, 1995; Fovell et al., 2006). The first term represents stability and usually dominates, but the second term (shear curvature) can be of similar magnitude when vertical wind shear changes sharply with height (Ghanmi et al., 2020). The Froude number Fr can be used to identify the relationship between gravity waves and terrain, defined as:

$$F_r = \frac{U}{Nh} \tag{4}$$

where *U* is the wind speed passing through the terrain and *N* represents the Brunt-Väisälä frequency. Resonance will occur and large-amplitude mountain waves will be excited when airflow passes over terrain with *Fr* close to 1 (Hunt, 1980; Chu and Lin 2000; Xu et al. 2021).

To diagnose the propagation of long-lasting, horizontally gravity waves, the atmospheric conditions must align with the wave-ducting hypothesis (Lindzen and Tung, 1976). Wave-ducting refers to gravity waves traverse horizontally within a stable atmospheric stratum, flanked by two reflective surfaces. The ducting of gravity waves is termed the ducting stable layer, characterized by enhanced stability. The upper reflective boundary is denominated the reflecting layer, which possesses comparatively weaker stability than the ducting layer, while the lower reflective boundary typically represents the ground. The reflecting layer reflects the upward-transmitted wave energy downward, while the ground reflects downward-propagating wave energy upwards, enabling the gravity waves to propagate horizontally with minimal energy dissipation. Moreover, if a critical layer (where wave speed approximates the primary flow velocity) or a Richardson number, *Ri* is less than 0.25 exists in the reflecting layer, it will enhance the reflection of wave energy and further reduce the energy of gravity waves spreading outward (Booker and Bretherton, 1967; Lindzen and Tung, 1976). The intensity of turbulence is represented by the local gradient Richardson number Ri, with a smaller Ri indicating stronger turbulence. It is defined as:

$$Ri = \frac{N_m^2}{\left(\frac{\partial \overline{U}}{\partial z}\right)^2} \tag{5}$$

where N_m^2 is the moist Brunt–Väisälä frequency squared and $\overline{U}$ is the mean wind speed along the wave propagation direction. The intrinsic phase speed in wave-ducting is defined as:

$$C_{d,n} = \frac{N_m D}{\left(\frac{\pi}{2}+n\right)} \tag{6}$$

where *n* indicates different vertical wave modes and *D* is the depth of the lower stable layer.

To calculate the momentum, energy, and heat fluxes generated by gravity waves, we follow the method proposed by Kruse & Smith (2015). First, the 2D meteorological fields are decomposed into background and disturbance fields to remove non-periodic synoptic-scale variations. Second, a high-pass filter with a cutoff wavelength of 200 km is applied to obtain the perturbation field specific to gravity wave activity scale. Third, gravity wave fluxes are computed by multiplying disturbance quantities at each grid point. Last, to reduce noise, a low-pass filter with a cutoff wavelength of 50 km is subsequently applied to the computed gravity wave fluxes. The vertical momentum flux (MF_z), energy flux (EF_z), and heat flux (HF_z) of gravity waves are defined as:

$$MF_z = \overline{\rho} u' w' \tag{7}$$

$$EF_z = p' w' \tag{8}$$

$$HF_z = \overline{\rho} c_p (w' T') \tag{9}$$

where u', w', p', and T' represent disturbances in horizontal wind, vertical wind, pressure, and temperature obtained from the second step, ρ is air density. For stable linear mountain waves, domain-averaged gravity wave energy and momentum fluxes satisfy the following relationship:

$$\overline{EF_z}(z) = -\overline{u}(z)\overline{MF_z} \tag{10}$$

According to equation (10), $\overline{EF_z}(z)$ will vary with height, proportional to $\overline{u}(z)$. Therefore, differentiating the above equation with respect to height z gives the relationship between energy flux divergence and background wind shear:

$$\frac{d\overline{EF_z}}{dz} = -\overline{MF_z} \cdot \frac{d\overline{u}}{dz} \tag{11}$$

When the wind shear $\frac{d\overline{u}}{dz} > 0$, if the wave causes upward momentum transfer ($\overline{MF_z} > 0$), it will lead to the convergence of gravity wave energy flux ($\frac{d\overline{EF_z}}{dz} < 0$), which causes energy to be converted from perturbation wave energy to mean kinetic energy (Zhang et al., 2001).

2.3. Experiment Design

The WRF model version 4.3.1 (Skamarock et al. 2021) is employed in this study. The simulation period was from 20 UTC 19 July to 20 UTC 20 July 2021. The three nested simulation domains are shown in Figure 1a, with horizontal resolutions of 27, 9, and 3 km respectively. The orange line on the map represents Henan Province, and the black dot indicates the location of the rainfall center (Zhengzhou station). There were 51 vertical levels, with the highest level at 50 hPa. The parameterization schemes employed in this study are the WSM6 microphysics (Hong and Lim 2006), YSU planetary boundary layer (Hong et al. 2006), RRTMG shortwave and longwave radiation (Iacono et al. 2008), and Kain-Fritsch cumulus schemes (applied only in D01 and D02) (Kain, 2004; Wang et al., 2019).

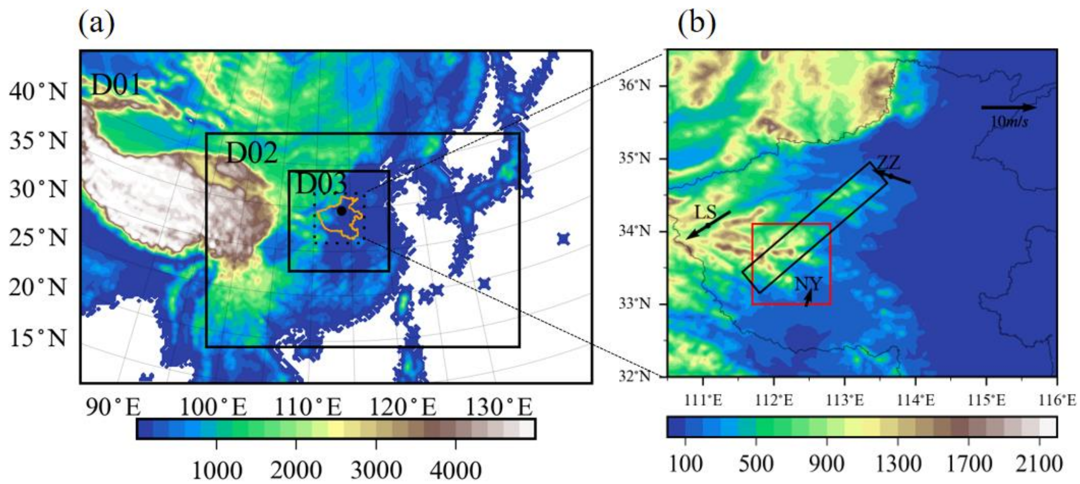

Figure 1. WRF model domain configuration and research area. (a) Configuration of the WRF model domains (D01, D02, and D03) and terrain elevation distribution (m; shaded) within the region, with the orange solid line representing main precipitation area (the range of Henan Province) and the black dot signifying the location of the precipitation center of Zhengzhou; (b) Terrain elevation (m; shaded) of heavey rain region (Henan Province), with black arrows indicating the wind speed and direction at a 900hPa height before the extrem houly precipitation occurred (July 20, 2021, 08:00). The sounding station location of Zhengzhou, Lushi, and Nanyang are denoted by “ZZ”, “LS”, and “NY”, respectively. The black box emphasizes the area of band rainfall, as the red box marks a particular region, Mountain Funiu, utilized in the terrain sensitivity experiments addressed later.

To obtain better understand of heavy rainfall evolution, the three-dimensional variational assimilation system of WRF was used to assimilate the sounding and surface observation data from China meteorological stations in the initial condition. To enhance the depiction of terrain accuracy, the high-resolution terrain is substituted with SRTM (Shuttle Radar Topography Mission) version 4.1 Digital Elevation Model (DEM) data, which boasts a resolution of approximately 90 meters. To account for sub-grid scale vertical momentum transport caused by sub-grid terrain, we activated the gravity wave drag option (gwd_opt=3) in the boundary layer scheme. This option comprehensively accounts for the effects of sub-grid scale gravity wave drag, blocking drag, small-scale gravity wave drag, and turbulent form drag (Beljaars et al. 2004; Kim and Doyle 2005; Kim and Arakawa 1995; Steeneveld et al. 2008).

To quantify the effects of gravity waves on extreme rainfall, two sets of terrain sensitivity experiments (Table 1) were designed. In these experiments, the terrain elevation of the FNM (indicated by the red box in Figure 1b) in WRF was altered to 1.5 or 0.5 times its original value to generate different intensities gravity waves.

Table 1. Experiments design

Experiment	Terrain	Purpose
CTL	Model default terrain	The model's capacity to replicate extreme precipitation
Terrain1.5	The terrain elevation was increased by a factor of 1.5	The impact of orographic gravity waves
Terrain0.5	The terrain elevation was reduced to 50% of its original height	The impact of orographic gravity waves

3 Convection and gravity wave activities

Figure 2 illustrates the circulation and low-level water vapor transport of the “21.7” event based on ERA5 data, from 08:00 on July 17, 2021, to 08:00 on July 20, 2021 (China Standard Time, CST). The analysis of the 500 hPa geopotential height field indicates a stable large-scale circulation situation from the 17th to the 20th July during the event, the western Pacific sub-tropical high and continental high pressure formed a steady saddle-shaped field around Henan province, which was conducive to sustainable precipitation. The strong pressure gradient between the western Pacific sub-high and the typhoon "In-fa" led to a robust southeast airflow, resulting in the transportation of water vapor from the Pacific region towards Henan. On the 20th July, this water vapor transport reached its peak. These stable circulation patterns and efficient water vapor transport provided the favorable background conditions to the occurrence of super-strong rainfall in the Henan area.

Figure 3a and 3b show the observed and simulated (from the CTL experiment) cumulative rainfall distribution of July 20, 2021. The observed precipitation primarily concentrated in the central and northern parts of Henan province, Zhengzhou city, where the heaviest daily rainfall exceeded 600 mm. Additionally, a band-like distribution precipitation (indicated by the black rectangle in Figure 3a) exists on the southwest side of the precipitation center. The CTL experiment successfully simulated the extreme precipitation at the rainstorm center and the band-like precipitation southwest of the rainfall center (indicated in the black rectangle in Figure 3b). Figure 3c provides the time series of the precipitation. The observed precipitation at the Zhengzhou station peaked at 201.9 mm between 16:00 and 17:00 on the 20th July, breaking the record for rainfall intensity in inland China. In terms of the area mean precipitation (the area indicated by the blue rectangle in Figure 3a), the observed rainfall (the black contour lines in Figure 3c) exceeded 25mm between 14:00 and 15:00. The simulated rainfall (the black dashed line in Figure 3c), exhibiting a relatively close magnitude to the observations, although with slightly advanced occurrence time. The CTL experiment effectively reproduced the spatial and temporal distribution characteristics of the "21.7" event.

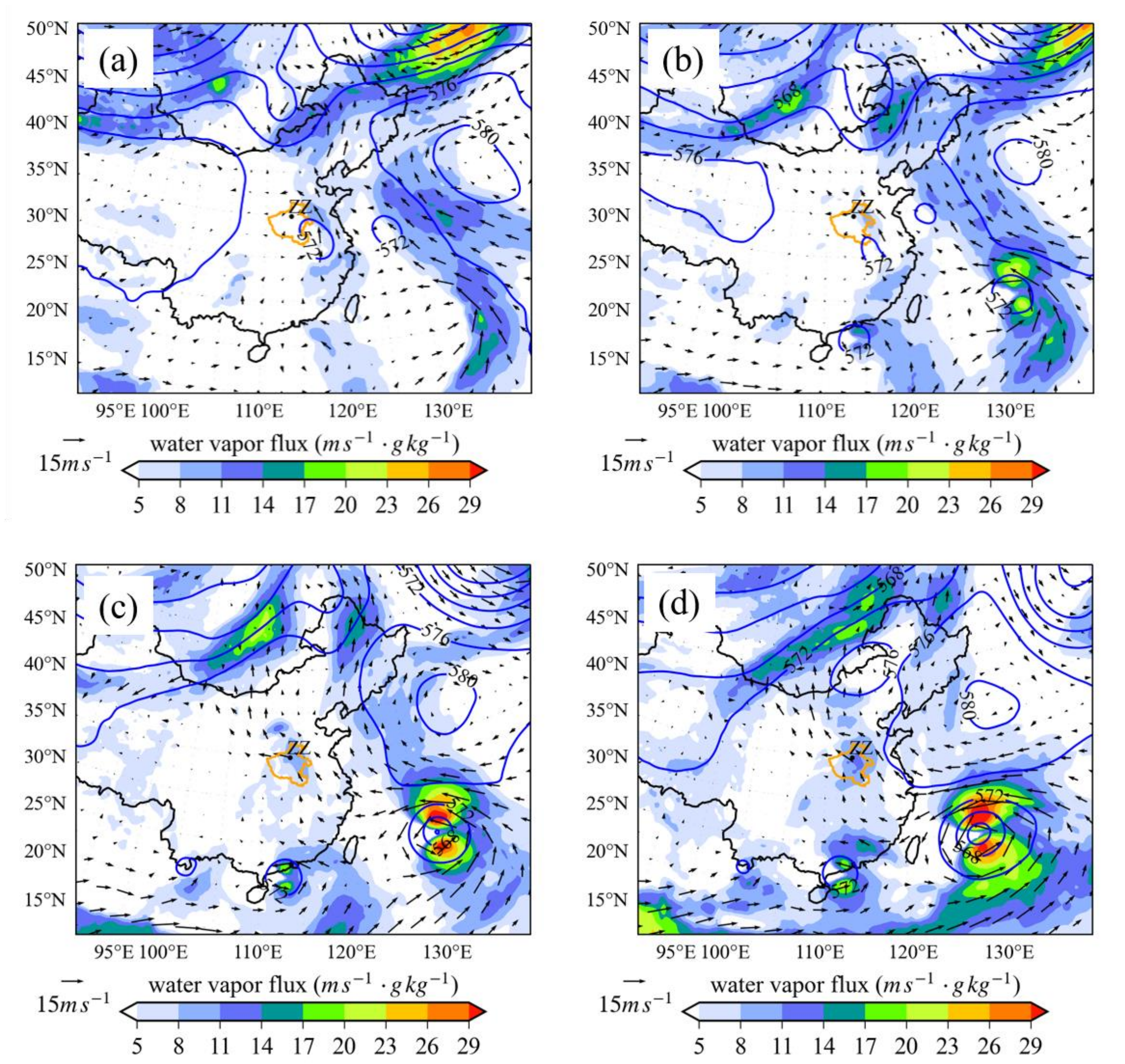

Figure 2. Evolution of atomospheric circulation during the "21.7" rainstorm. The geopotential height at 500 hPa (blue contours), wind vectors and moisture flux values (shaded) at 850 hPa at 08:00 CST on (a) July 17, (b) July 18, (c) July 19, and (d) July 20, 2021. The orange outline denotes the boundary of Henan Province (the main precipitation area for the rainstorm), while the black dot marked "ZZ" denotes Zhengzhou city's location (the center of the rainstorm).

To understand the convective activity during the rainstorm, Figure 4 presents the evolution of radar composite reflectivity from 12:00 to 17:00 on July 20, 2021. As seen in Fiugre4, the QSCS (>50 dBZ) initially occurred in the center of the heavy rainfall event (indicated by black dot in Figure 4) at 12:00 on the 20th July, and reached its peak from 16:00 to 17:00. Concurrently, convective cells began to form southwest of the rainstorm center (south west of the black rectangle in Figure 4). The convective cells gradually developed to the northeastern direction, displaying a band-like convection (Figures 4b, c, and d). Then, the convective cells merged with the QSCS in the rainfall center from 16:00 to 17:00 (Figures 4e and f). The combination of the convective cells and the QSCS is crucial to the enhancement and maintenance of the QSCS (Wei et al., 2023; Sun et al., 2023). Therefore, the focus of this study will be on the development of this band convection activity, which started at 12:00 and gradually subsided after 17:00, lasting for over 5 hours.

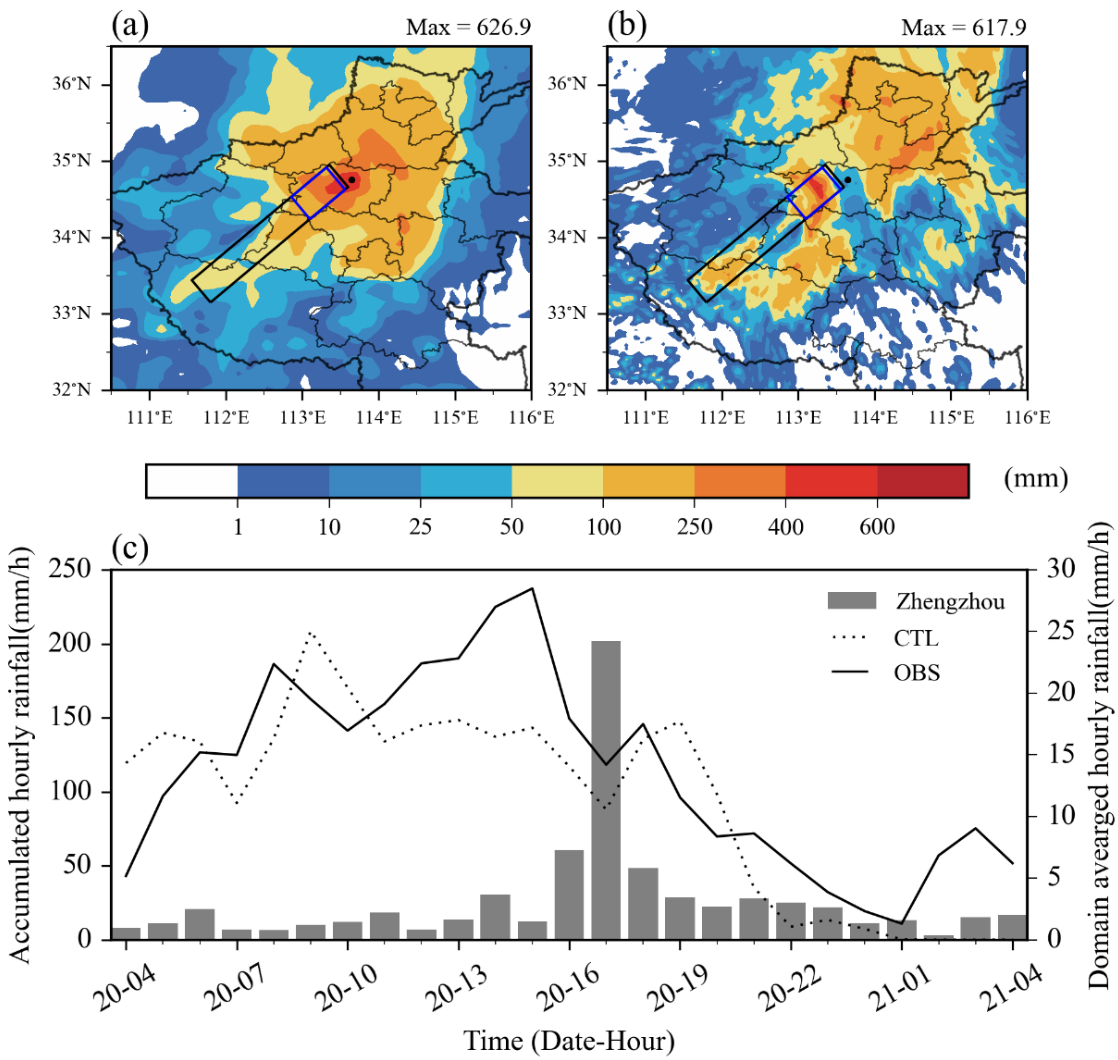

Figure 3. Spatial distribution of accumulated precipitation and hourly rainfall time series. (a) Observed and (b) CTL experiment's spatial distribution of accumulated precipitation (contour fill) over a 24-hour period from 08:00 CST on July 20 to 08:00 CST on July 21, 2021. (c) Time series of hourly rainfall (mm h^{-1}) at the Zhengzhou station (bar graph) and in the core area of rainfall (line graph). The black and blue box in Figure 3a and 3b denotes the band rainfall region, and the core rainfall area, respectively.

Figure 5 shows that the simulated horizontal distribution and evolution characteristics of radar composite reflectivity from the CTL experiment. Spatially, the CTL experiment successfully reproduces the QSCS in rainfall center and the band convection southwest of the rainfall center, with a slightly southwest location bias. Temporally, the convection initiated at 12:00 (Figure 5a) and gradually moved to the northeastern, eventually dissipating at 17:00 (Figure 5f). The evolution of the simulated convective cells is in accordance with observation, with a few hours advanced. Overall, the CTL experiment effectively simulated the progression of precipitation and convective systems throughout the "21.7" event.

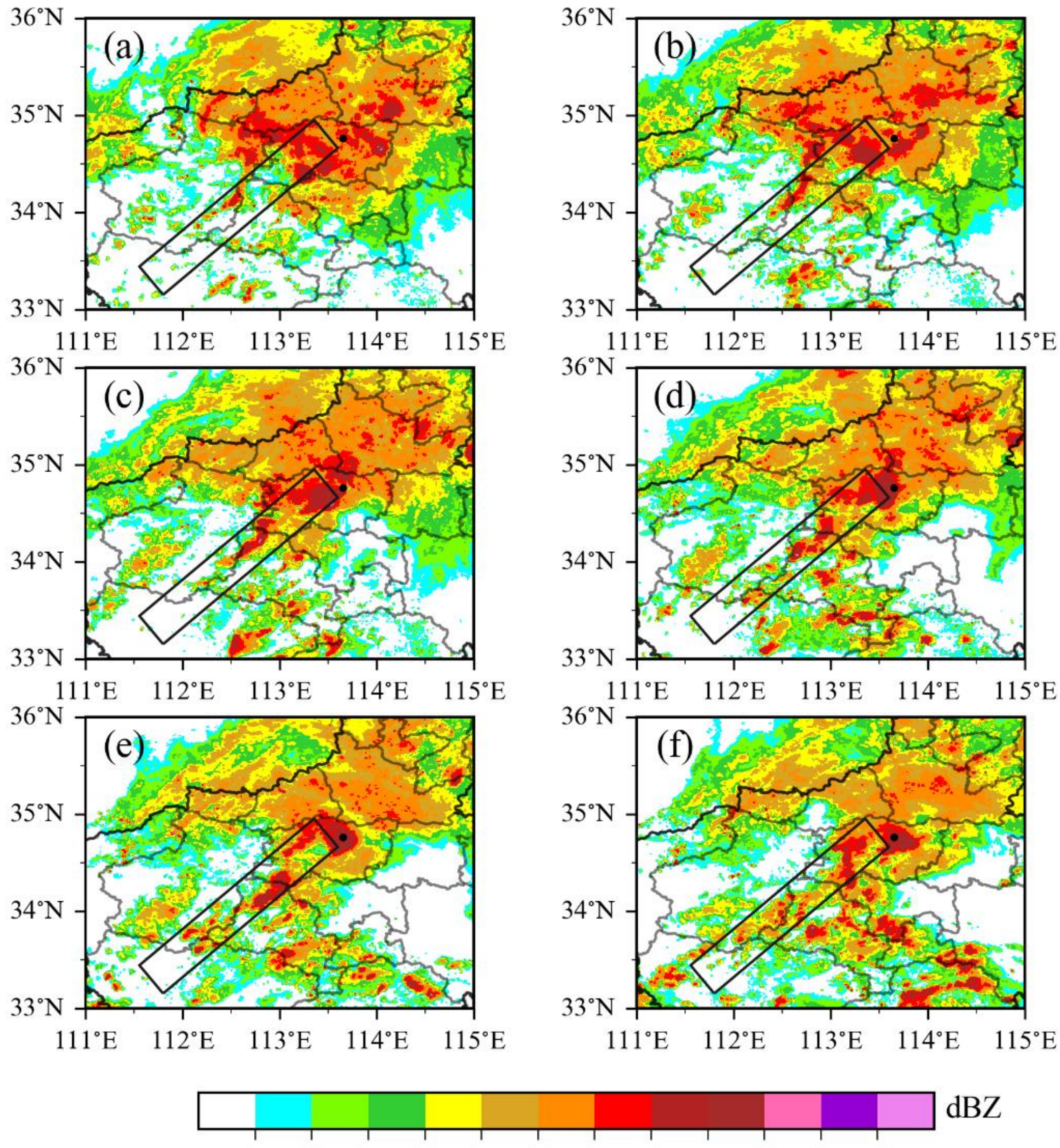

Figure 4. Evolution of observed composite radar reflectivity (shading, units: dBZ) in heavey rainfall region(Henan Province) at (a) 1200, (b) 1300, (c) 1400, (d) 1500, (e) 1600, and (f) 1700 CST on July 20, 2021. The black box (same as in Figure 3a) indicates the area of the convective bands, the black line represents the border of Henan Province, the black point indicates the location of Zhengzhou City.

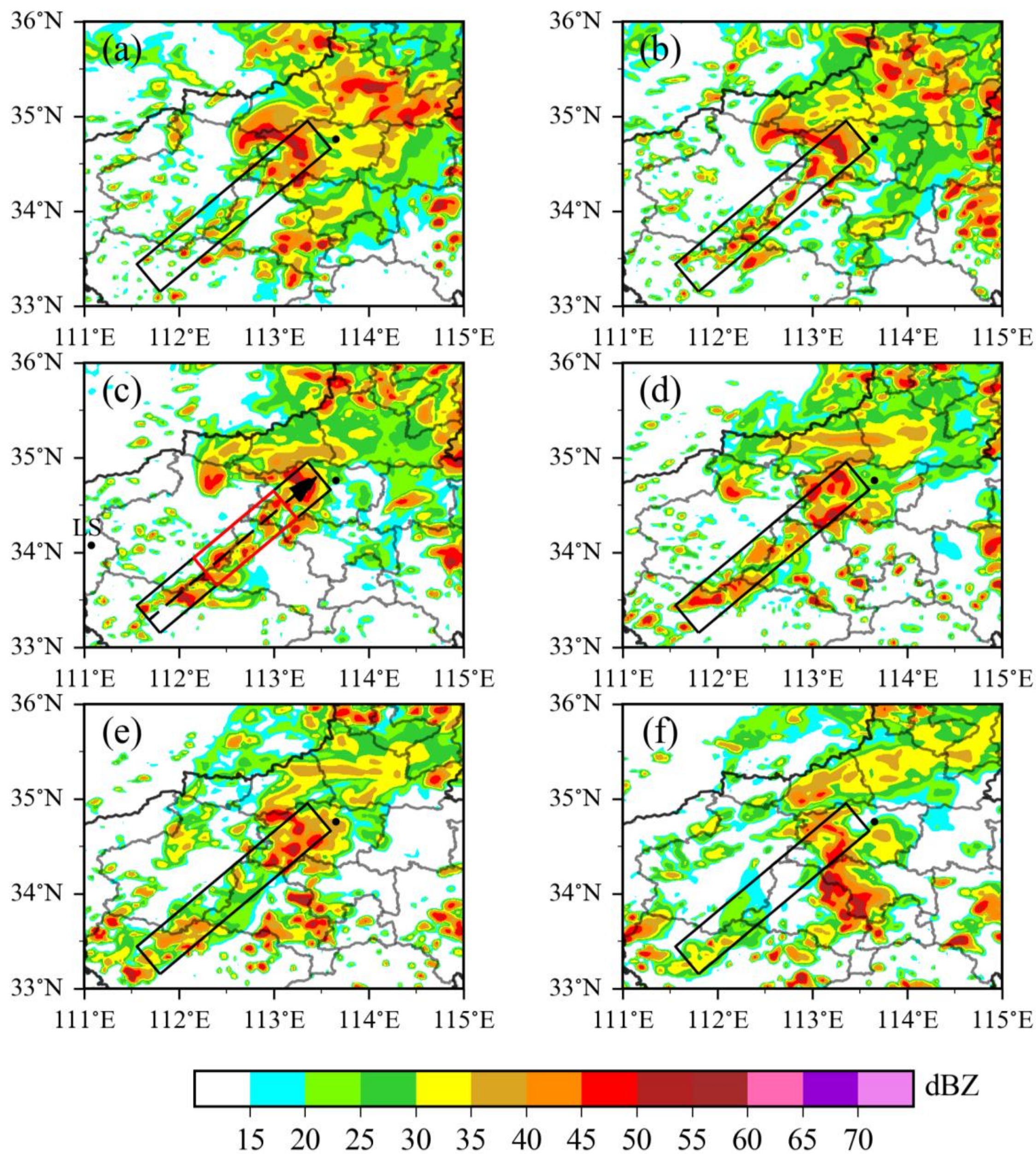

Figure 5. Simulated radar composite reflectivity (shading, units: dBZ) over research area at (a) 1200, (b) 1300, (c) 1400, (d) 1500, (e) 1600, and (f) 1700 CST on July 20, 2021. The black box highlights the same area as shown in Figure 4. The red rectangle in Figure 5c indicate the primary of the gravity activity.

4 Case overview and simulation

Section 3 indicates that, as the convective cells propagate, a band-like convection between the FNM and the rainfall center was triggered. Due to the band-like convection is probably related to gravity wave activity. This section will firstly concentrate on the movement characteristics of the band-like convection, aiming to explore the relationship between gravity waves and the convective cells southwest of the rainfall center. Subsequently, an assessment of atmospheric stability conditions will be conducted to ascertain their conduciveness to the triggering and propagation of gravity waves. Finally, the influence of the gravity wave on the extreme precipitation will be discussed.

4.1. Banded convection

To understand the relationship between gravity wave activity and the convective cells southwest of the rainfall center, the vertical structure of band convection related to the convective cells was analyzed. Figure 6 illustrates the distance-height vertical cross-section of cloud-water mixing ratio from the CTL experiment. Within the red rectangular frame in Figure 6e, two convective systems extending beyond 6 km can be seen. The convective regions situated between the terrain and the rainfall center with horizontal spacing distance about 60 km for one convective region located 100 km from the starting point of the profile and another at 160 km. The convection initiation occurred at 12:00 on July 20, 2021, originating from the FNM (Figure 6a). Subsequently, it gradually deepened and propagated northeastward (Figure 6b~e), and started to dissipate at 18:00 on July 20, 2021 (Figure 6f). The banded convection between the terrain and the rainfall center persisted for over 6 hours and extending over 60 km, which could potentially be attributed to the vertical airflow induced by gravity wave activity.

To understand the wave characteristics of the convective cells southwest of the rainfall center, following Wheeler and Kiladis (1999), the frequency-wavenumber spectrum of the cloud water mixing ratio at a height of 5 km is calculated (Figure 7). From Figure 7b, it can be observed that the phase speed c of the gravity activity is approximately 10 m s^{-1}, the wavelength is about 60-90 km, and the period is about 90-160 min. In addition, the wave speed c is unrelated to the horizontal wavelength (wavenumber k), indicating that this wave is a non-dispersive wave. These two characteristics are consistent with the characteristics of mesoscale gravity waves (Nappo, 2013; Buijsman et al., 2019), suggesting that the convective cells are related to mesoscale gravity waves.

Analysis in section 4.1 reveals that the banded convection composed by convective cells between the rainfall center and the terrain is related to mesoscale gravity wave activity. The vertical updraft of the convective cells exhibits wave-like features, with a phase speed of approximately 10 m s^{-1}, a wavelength of 60-90 km, and a period of 90-150 minutes.

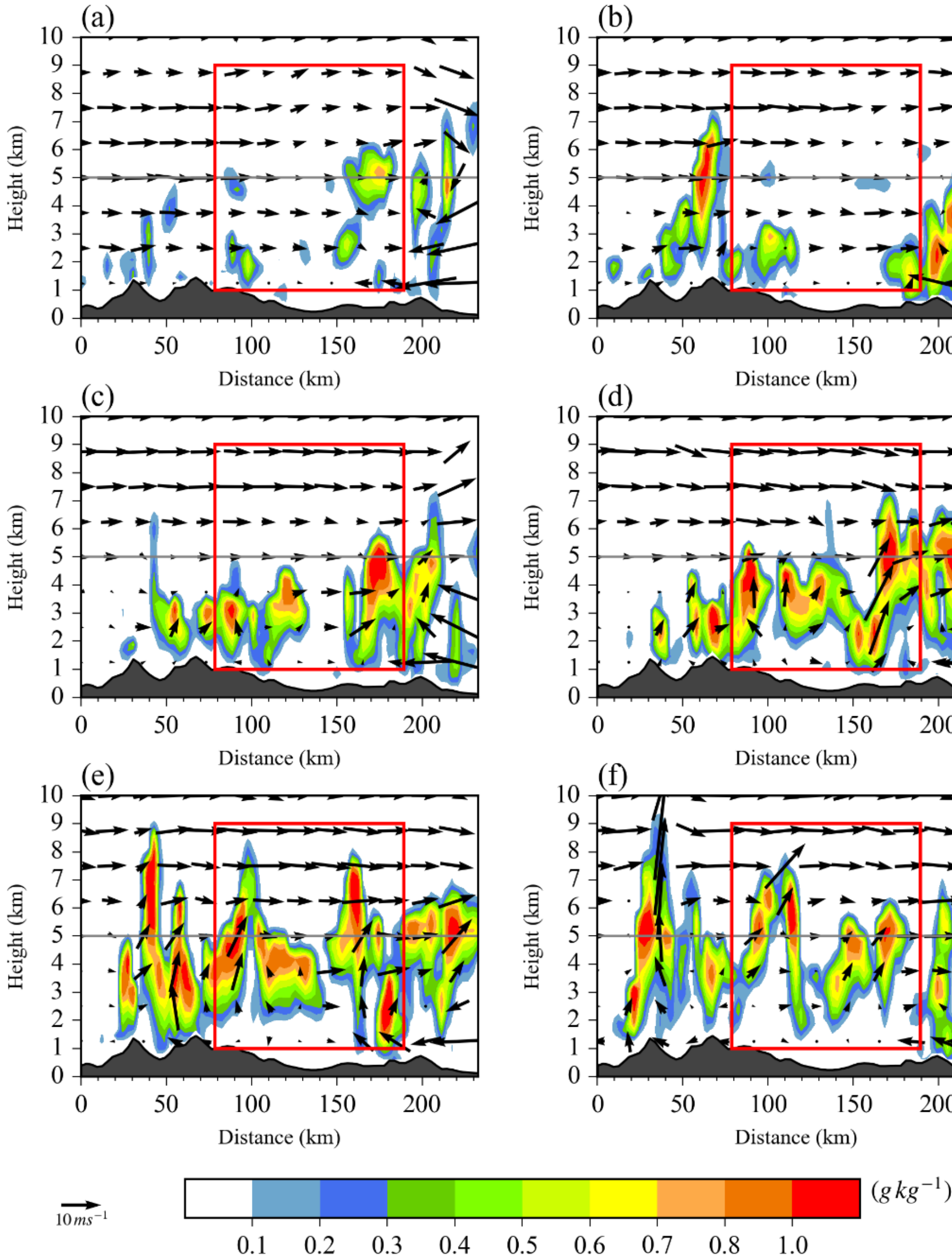

Figure 6. Temporal evolution of the vertical cross-section of cloud water mixing ratio (color-filled; g kg-1) and synthesized wind (vertical speed magnified 5 times; m s^{-1}) in the CTL experiment at (a) 1000, (b) 1100, (c) 1200, (d) 1300, (e) 1400, and (f) 1500 CST on July 20, 2021. The alignment of the cross section follows the direction of the black dashed arrow in Figure 4c. The red rectangle, consistent with Figure 4c, indicates the primary locations of gravity wave activity.

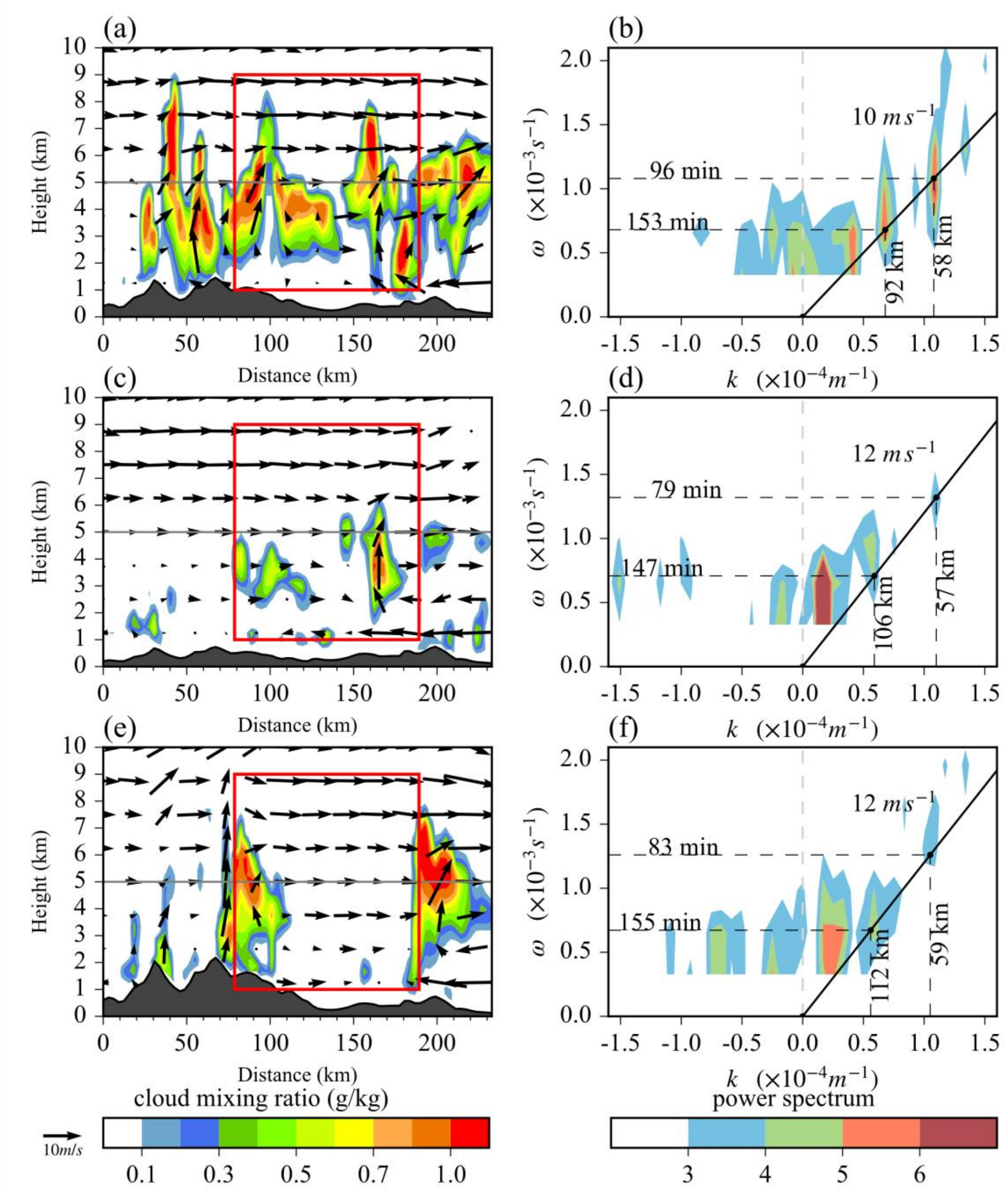

Figure 7. Comparative analysis of gravity wave intensity and phase speed across different terrain height sensitivity experiments. The wave-parallel vertical cross-sections of cloud water mixing ratio (shading; g kg^{-1}) and wind component along the same cross-section as in Figure 5 at 1400 CST on July 20, 2021 are presented in experiments (a) CTL, (c) Terrain05, and (e) Terrain15. The power spectra of the cloud mixing ratio at an altitude of 5 km along the same line are displayed in experiments (b) CTL, (d) Terrain05, and (f) Terrain15. In Figure 7b,d,f ,the solid black line represents the phase speed ω/k, the black dashed lines indicate the horizontal wavelengths and wave periods corresponding to the peaks.

4.2. Gravity wave generation and propagation

In section 4.1, banded convection south west of the rainfall center was considered related to the gravity wave, which persisting for over 6 hours and extending over 60 km. However, the triggering and propagation mechanisms of these long-lasting, horizontally propagated gravity waves remain unclear. Therefore, we will diagnose the atmospheric conditions to assess if the gravity wave could be excited, then explore the mechanisms of gravity wave propagation.

To diagnose the excitation of gravity wave, Figure 8 illustrates the vertical profiles of atmospheric stability conditions between the FNM and rainfall center during the event. The area-averaged moist Brunt-Väisälä frequency squared N_m^2 (Figure 8a), the squared Scorer parameter l^2 (Figure 8b), and the wind speed parallel to wave propagation $\overline{u}$ (Figure 8c), within the gravity wave activity area (indicated by the red rectangle in Figure 5c) are shown. These profiles are based on the results of the CTL experiment and observations from the "Lushi" sounding station. The abrupt increase in wind speed $\overline{u}$ with height, resulting in strong vertical wind shear (Figure 8c), and the significant decrease in l^2 between 6-8 km altitude (Figure 8b), suggesting that atmospheric conditions favor the triggering of horizontally propagating gravity waves. Additionally, the N_m^2 peaks between heights of 5-9 km (Figure 8a), indicating a relatively more stable atmosphere in this range, conducive to the formation of ducted gravity waves.

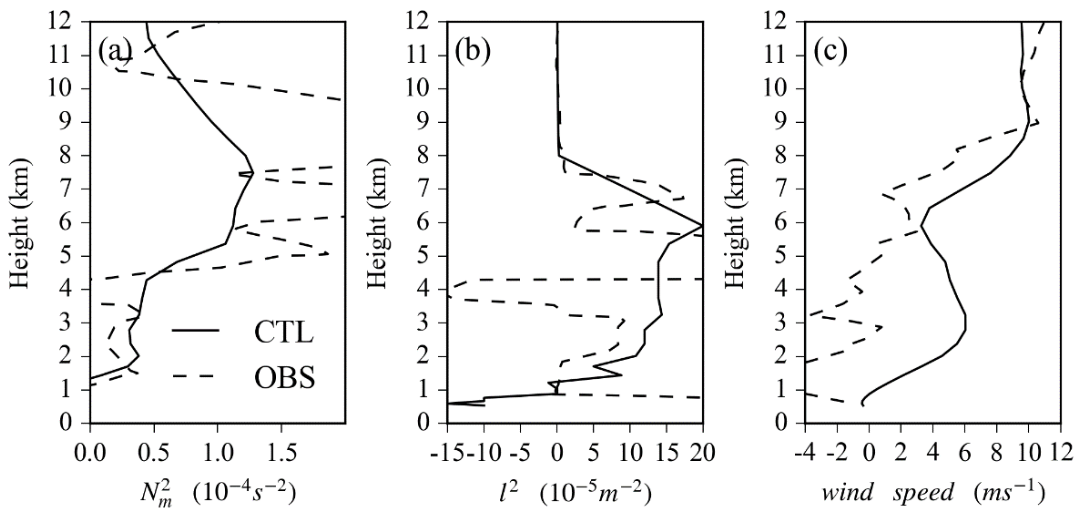

Figure 8. Diagnosis of stability conditions during the excitation of gravity wave. Vertical profiles of (a) square of moist Brunt–Väisälä frequency, (b) the scorer parameter and (c) wind speed in southwesterly direction averaged in red region of Figure 5c. The solid line represent the results caculated from CTL experiment at 1400 CST 20 July 2021, while the dashed line represents observation from Lushi station (indicated as “LS” in Figure 5c) at 0800 CST.

Although the atmospheric conditions were favorable for the excitation of gravity wave, the source of the gravity wave during the "21.7" event remains unclear. One possible source of the gravity wave is the FNM, for the gravity wave just located at the lee ward slope of the terrain. To investigate the connection between the gravity wave and the terrain, we calculated the Froude number (*Fr*) using Eq. (4). Figure 9 presents the *Fr* distribution for different terrain height sensitivity experiments. For the CTL experiment (Figure 9a), the *Fr* ranges from 0.5 to 1.5 over the FNM, indicating a favorable condition for mountain wave excitation (Hunt, 1980; Chu and Lin, 2000; Xu et al., 2021). Considering the strong vertical wind shear shown in Figure

8c, it can be suggested that when the southwest flow in front of the MCV passes through the northwest-southeast direction FNM, the strong vertical wind shear and buoyancy disturbances would be generated, and subsequently the quasi-steady orographic gravity waves (mountain waves) would be triggered.

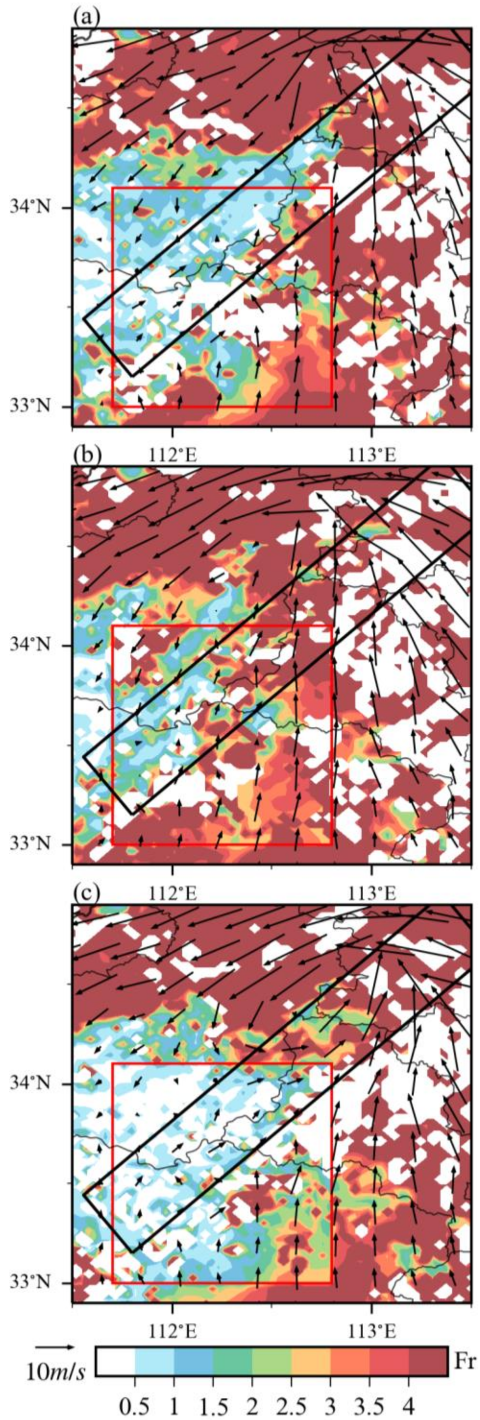

Figure 9 Comparative analysis of spatial distribution of Froude number F_r across different terrain height sensitivity experiments. (a) CTL, (b) Terrain0.5, (c) Terrain1.5 experimen's Froude number (shaded) and wind vector (vectors; units: $\mathrm{m\ s^{-1}}$) at 1200 CST on July 20, 2021.

The Froude number estimated from the altitude range of 500m to 1500m. The blcak and red box are same as in Figure 1b.

To analyze the propagation of the gravity wave, wave-ducting hypothesis should be satisfied, for the gravity waves are long-lasting, horizontally propagated waves during "21.7" event (Lindzen and Tung, 1976; Bosart et al., 1998; Kusunoki et al., 2000). To analyze whether the wave-ducting hypothesis is satisfied, atmospheric stability along the gravity wave propagation path was diagnosed. Figure 10 illustrates the vertical cross-section of the moist Brunt-Väisälä frequency (green and blue contour lines), the critical layer (red contour line), and $Ri < 0.25$ area (gray shading). The position and direction of the cross-section indicated by the dashed arrows in Figure 5c. The results reveal the existence of a relatively stable atmospheric layer (ducting stable layer) between 5-9 km altitude along 50-170 km horizontal distance. Above the ducting layer lies a reflecting layer which has low stability, extending above 8 km and reaching approximately the top of the tropopause. In addition, in the reflecting layer, there are also exists critical layers (red contour line at approximately 8 km altitude) and areas with $Ri <$ 0.25 (gray shaded area), which enhance the reflection effect of reflecting layer.

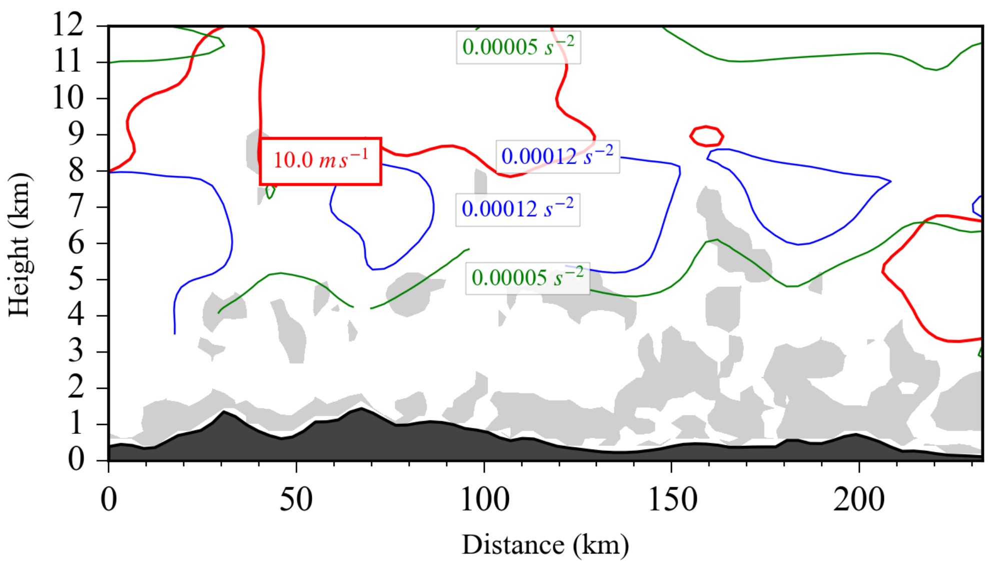

Figure 10. Wave-parallel vertical cross-section of the square of moist Brunt–Väisälä frequency N_m^2 (s^{-2}; contour) along the wave-fronts depicted by the dashed black arrow showed in Figure 4c at 1400 CST 20 July 2021. The gray shading indicates Richardson number Ri <0.25 and the red line shows the critical level (wave speed equals to the horizontal wind speed) , assuming the wave speed is 10 m s^{-1}.

According to Eq. (6), under the primary mode ($n = 0$), given the depth of the stable layer D is 1 km and the averaged N_m in the stable layer is 0.011 s^{-1} (Fiugre8). Considering the calculated ground-relative wave phase speed is ~6.9 m s^{-1} (Figure 9a), the mean background wind in the wave-parallel direction in the stable layer is ~4 m s^{-1} (Figure 9c), the relative ground wave velocity is calculated to be 10.9 m s^{-1}, which is consistent with the simulated ground-relative wave phase speed of around 10 m s^{-1} (Figure 7b). The inherent wave velocity of the wave channel matches the actual wave velocity, providing further confirmation of the existence of wave-ducting in the troposphere in the "21.7" process. These conditions are favorable for wave-ducting (Lindzen and Tung, 1976), therefore, it can be considered that the stability conditions are conducive to the long-lasting, horizontally propagated gravity wave.

The stable atmospheric stratification during the "21.7" event was favorable for the excitation and horizontal propagation of the quasi-steady gravity waves. The environment provides a wave duct for these gravity waves, with a thick stable layer between 5-9 km. This gravity wave is a type of orographic gravity waves. The process of these gravity waves generation and propagation can be summarized as follows: when the southwest airflow in front of the MCV passed through the FNM, a strong wind shear was created for the friction and blocking effects of the terrain. The strong wind shear lead to a sudden decrease in l^2 and the triggering of orographic gravity waves. And then, due to the wave-ducting effect between the terrain and the rainfall center, the gravity wave can propagate horizontally over more than 60 km distance, and trigger band-like convective cells, which is manifested as a banded convection.

4.3. Effects of gravity waves on extreme rainfall

Due to the significantly enhancement of these convective cells related to the banded convection on the extreme rainfall over the rainfall center (Wei et al., 2023; Sun et al., 2023), the gravity waves may likely enhance extreme rainfall over the center. However, the magnitude of the effects of gravity waves on extreme rainfall and the mechanisms are still unknown. Sensitive experiments were conducted by modifying the terrain heights of the FNM to produce gravity waves of differing intensities. These sensitivity experiments are summarized in Table 2. Then, the precipitation over rainfall center of different experiments was compared. Lastly, the mechanisms through which the gravity waves affected rainfall was analyzed.

To compare characteristics of gravity waves induced by different altitude terrain, Figure 7 shows the intensity of gravity wave simulated by different experiments. The CTL experiment had the most strengthen gravity wave amplitude (Figure 7b), while the sensitivity experiments both exhibited weaker amplitude compared to CTL experiment (Figure 7d, f). Examining the *Fr* distribution in Figure 9 for different terrain sensitivity experiments, it was observed that decreasing terrain height (Terrain0.5 experiment) lead to excessively high *Fr* over the FNM (Figure 8b). Conversely, increasing terrain height (Terrain1.5 experiment) resulted in an undesirably low *Fr* in the same region (Figure 8c). Both too high and too low *Fr* are unfavorable for mountain wave generation (Hunt, 1980; Chu and Lin 2000; Xu et al. 2021). Sensitivity terrain experiments both triggered more weaker amplitude gravity waves compared to the CTL experiments for too high or too low *Fr*.

To compare the effects of different amplitude gravity waves on the precipitation, Figure 11 presents the horizontal distributions of 24-h accumulated precipitation from the two sensitivity experiments, as well as their differences compared to the CTL experiment. The sensitivity experiments simulated extreme rainfall over the rainfall center with weaker magnitudes and shifted locations towards the southwest (Figure 11a, b) in compare to CTL experiment (Figure 3a). Meanwhile, sensitivity experiments showed less accurate simulation of the banded precipitation southwest of the rainfall center (indicated by black boxes in Figure 11a, b) compared to CTL experiment (indicated by black box in Figure 3a). These results suggest that altering the altitude of the FNM, weakened the gravity wave, decreased precipitation in the rainfall center, and disturbed the banded distribution of precipitation between the rainfall center and the terrain to some extent.

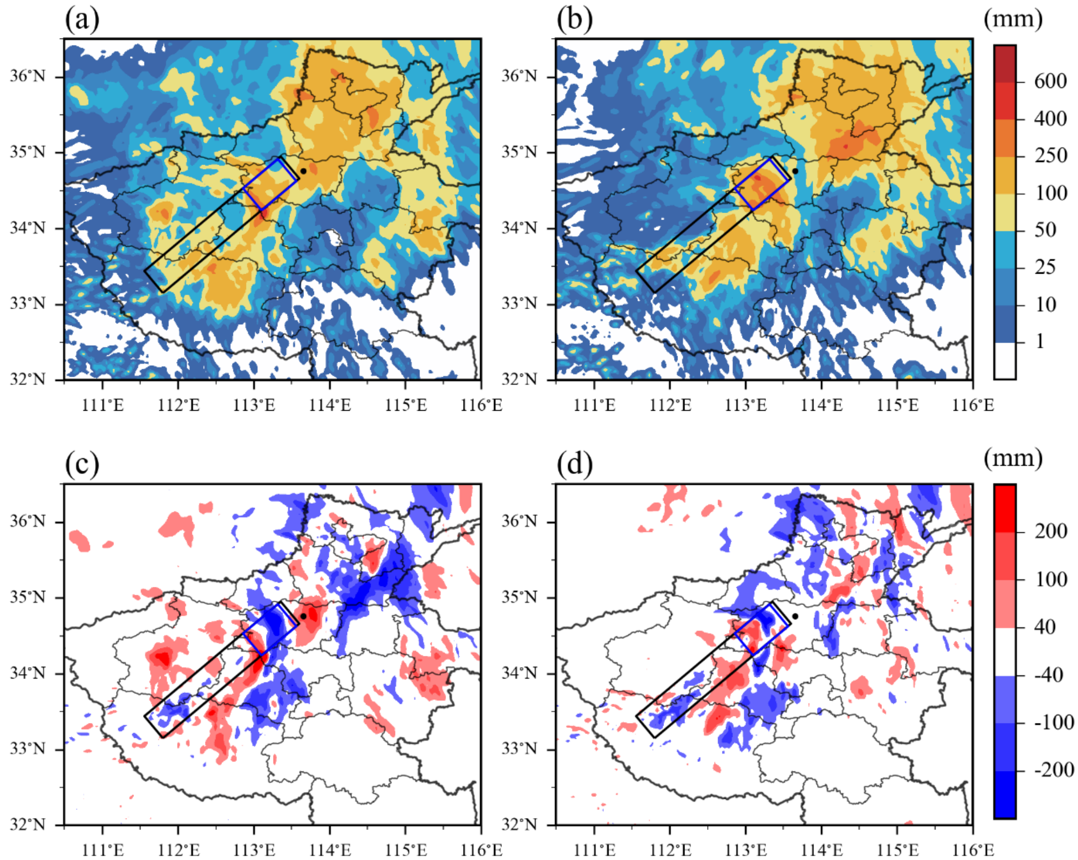

Figure 11. Comparative analysis of spatial distribution of raifall across different terrain height sensitivity experiments. Accumulated precipitation from (a)Terrain 0.5, (b) Terrain1.5 experiment, and their minus (c)Terrain 0.5-CTL, (d) Terrain1.5-CTL during a 24-hour period from 08:00 CST on July 20th to 08:00 CST on July 21st, 2021 .The black box (same as in figure 4) indicates the region of band rainfall , while the blue box represents the core area of rainfall.

Table 2 compares maximum precipitation amounts over different accumulation periods from the experiments. Both terrain sensitivity experiments, Terrain0.5 and Terrain1.5, almost all had lighter precipitation for all accumulation periods compared to CTL. The Terrain0.5 experiment showed over 30% lower rainfall for all periods compared to CTL. Similarly, the Terrain1.5 experiment also had more than 20% lighter precipitation, with only exception of 1 hour accumulated precipitation. These results demonstrate that gravity wave with lower intensity generated lighter precipitation. To put it another way, the gravity wave can enhance precipitation in the rainfall center by over 20%.

To illustrate the mechanisms by which gravity waves can enhance rainfall, Figure 12 shows the hourly rainfall evolution (Figure 12a), low-level divergence (Figure 12b), and gravity wave energy flux divergence (Figure 12c) time series over the rainfall center for different experiments. From the hourly precipitation evolution in Figure 12a, all experiments had lighter rainfall compared to observations, however, the CTL have more heavy precipitation. Correspondingly, CTL experiment also had stronger low-level divergence than the terrain sensitivity experiments (Figure 12b). The stronger rainfall and divergence in CTL experiment compared to the sensitivity experiments mainly occurred after 13 UTC on 20 July (Figure 12a, b), corresponding to the time when the gravity wave peak approached to the rainfall center (Zhengzhou) (Figure 6d), so enhancement of the gravity waves on the QSCS over the rainfall center began at this time.

Figure 13 illustrates the vertical profiles of momentum flux (MF_z), energy flux (EF_z), and heat flux (HF_z) induced by gravity waves over the rainfall center at 13 UTC on 20 July from different experiments. It can be observed that all experiments demonstrated gravity wave energy flux convergence ($\frac{d\overline{EF}_z}{dz} < 0$) around 1.5-3.5 km (Figure 13b), implying that wave energy was converted to mean kinetic energy in the lower of troposphere (Zhang et al., 2001), enhancing vertical motion there. According to Eq. (11), when wind shear $\frac{d\overline{u}}{dz} > 0$, upward momentum transport by wave disturbances ($MF > 0$) results in gravity wave energy flux convergence ($\frac{d\overline{EF}_z}{dz} < 0$). Consequently, the upward momentum flux (Figure 13a) and positive vertical wind shear (Figure 13d) were accountable for converting the wave energy to mean flow energy at lower troposphere. The low-level wave energy flux convergence was the primary cause of enhanced convection. Comparing to sensitive experiments, CTL had the strongest energy flux convergence at 13 UTC and afterwards (Figure 13b, Figure 12c), leading to the highest conversion of wave disturbance energy to convective kinetic energy below 5 km, consequently resulting in the strongest low-level divergence (Figure 12b) and heaviest rainfall (Figure 12a) compared to the sensitivity experiments.

It was also worth noting that there is strong positive heat flux over the rainfall center from the vertical profiles of heat flux in Figure 13c. According to the wave-conditional instability of the second kind (wave-CISK) hypothesis, gravity waves can trigger convergence of low-level flow and organize convection, while latent heat released by the convection can enhance gravity waves, forming a positive feedback loop that further invigorates convection in the region (Lindzen, 1974; Raymond, 1975). Among the three numerical experiments, CTL had the maximum heat fluxes, producing the strongest positive feedback, corresponding to the strongest simulated convection, further validating the enhancement effects of the gravity wave on convection.

Table 2. Maximum Cumulative Precipitation (mm) over rainfall center (indicated by the blue box Figure 11)

Duration	OBS	CTL	Terrain0.5	(Terrain0.5-CTL)/CTL	Terrain1.5	(Terrain1.5-CTL)/CTL
1h	201.9	127.8	94.3	-26%	139.3	9%
3h	333.2	278.2	179.7	-35%	220.5	-21%
6h	465.9	437.2	236.6	-46%	404.4	-8%
12h	556.0	611.3	347.7	-43%	468.5	-23%
24h	626.9	617.9	368.5	-40%	495.9	-20%

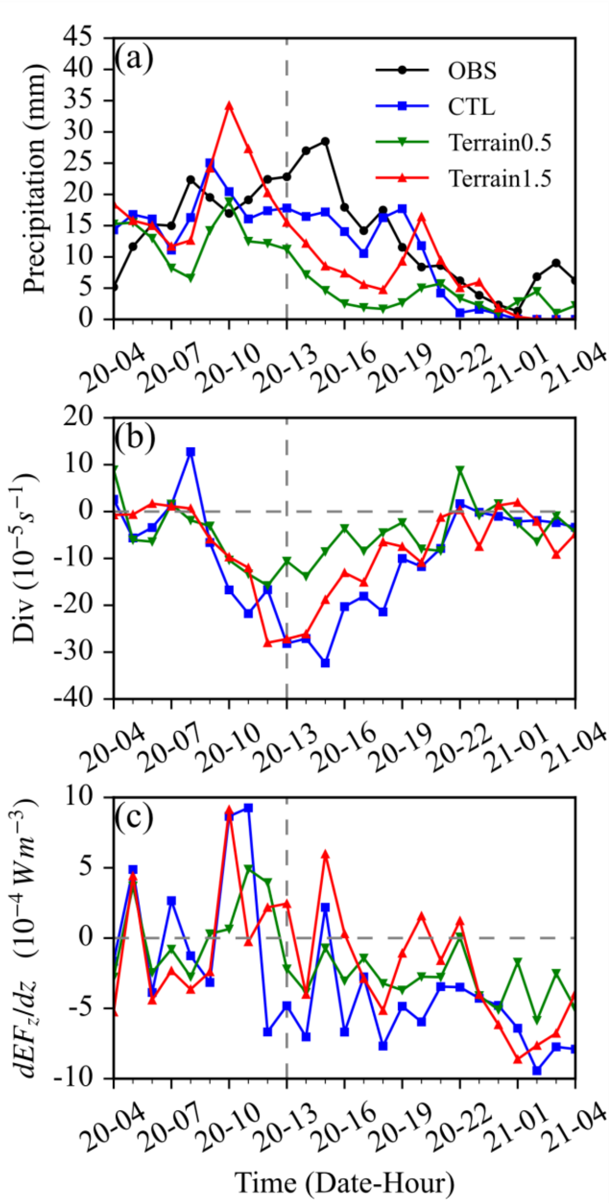

Figure 12. Evolution of precipitation and diagnositic related to gravity wave in the core area of rainstrom. (a) hourly precipitation, (b) divergence and (c) wave energy flux from 0800 CST, July 20th, to 0800 CST, July 21st, 2021. The data is spatially averaged in the area indicated by the blue box in Figure 10b. Divergence and wave energy flux are represented at a height of approximately about 1.5~6 km (corresponding to the 8~18 level of model output).

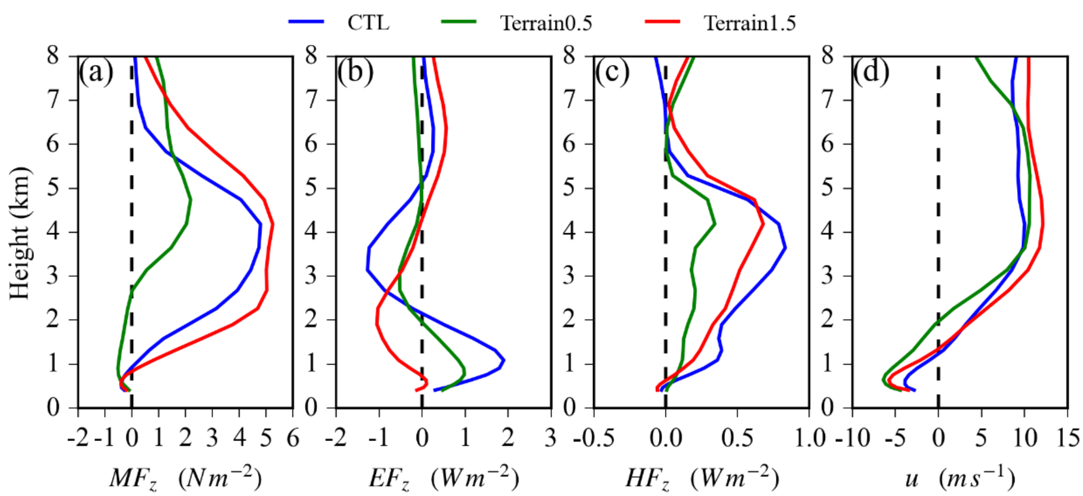

Figure 13. Vertical profiles of fluxes induced by gravity wave in the core region of storm. (a) momentum flux (MF_z), (b) energy flux (EF_z), (c) heat flux (HF_z) and (d) horizontal wind speed u along the wave front, averaged within the blue box in Figure 11b, at 1300 CST, July 21, 2021. The wind speed was projected onto the wave propagation direction (black arrows in Figure 4c).

To elucidate the process of gravity waves effect on convection at rainfall center. Figure 14 presents the vertical cross section of potential temperature perturbations and vertical velocity in the southwest–northeast direction through the rainfall center. The potential temperature perturbation serves as an indicator of air parcel buoyancy, where buoyancy $B = g\frac{\theta'}{\theta_0}$ in dry condition and $g\left(\frac{\theta_\rho}{\theta_{\rho 0}} - 1\right)$ in moist condition (Bryan & Fritsch, 2002; Schumacher, 2009). At 11:00 (Figure 14 a), in addition to the previously discussed gravity wave at the upper level of troposphere, a low-level gravity wave is also present. This low-level gravity wave was excited by latent heat in convection and tended to remain near its source rather than propagating away (Schumacher, 2009). At 11:40 (Figure 14b), unstable air parcels above the surface are lifted over the wave for the buoyancy of low-level gravity wave, attaining its level of free convection, and erupting into deep updrafts. As air parcels influenced by low-level waves ascend, they encounter buoyancy induced by high-level gravity waves, intensifying the convection process. The intense deep convection persists until 12:30 (Figure 14c), and gradually decrease at 13:00 (Figure 14d). The process of synergy between different levels of gravity waves is aligns with the wave energy flux in Figure 13b, the upper level gravity wave facilitates the downward transmission of wave energy, while the low-level gravity wave facilitates the upward transmission of wave energy. This synergy between gravity waves at high and low levels in the troposphere significantly contributes to the formation of intense deep convection, which often result in extreme precipitation events.

In section4.3, gravity waves are shown to be responsible for more than 20% of the rainfall intensity over the rainfall center. The process through which gravity waves affected rainfall was as follows: after propagating from the terrain to the rainfall center, downward dispersion of wave energy from high-level gravity waves, synergizes with upward wave energy produced by low-level gravity waves excited by latent heat at low levels. This synergy leads to the convergence of wave energy flux and intensifies ascending motion. To put it another way, the low-level gravity wave makes the parcel up to a middle level, and the high-level gravity wave make the parcel continue ascend, exhibit a “relay effect”. The synergy between different levels of gravity waves can trigger or enhance deep convection.

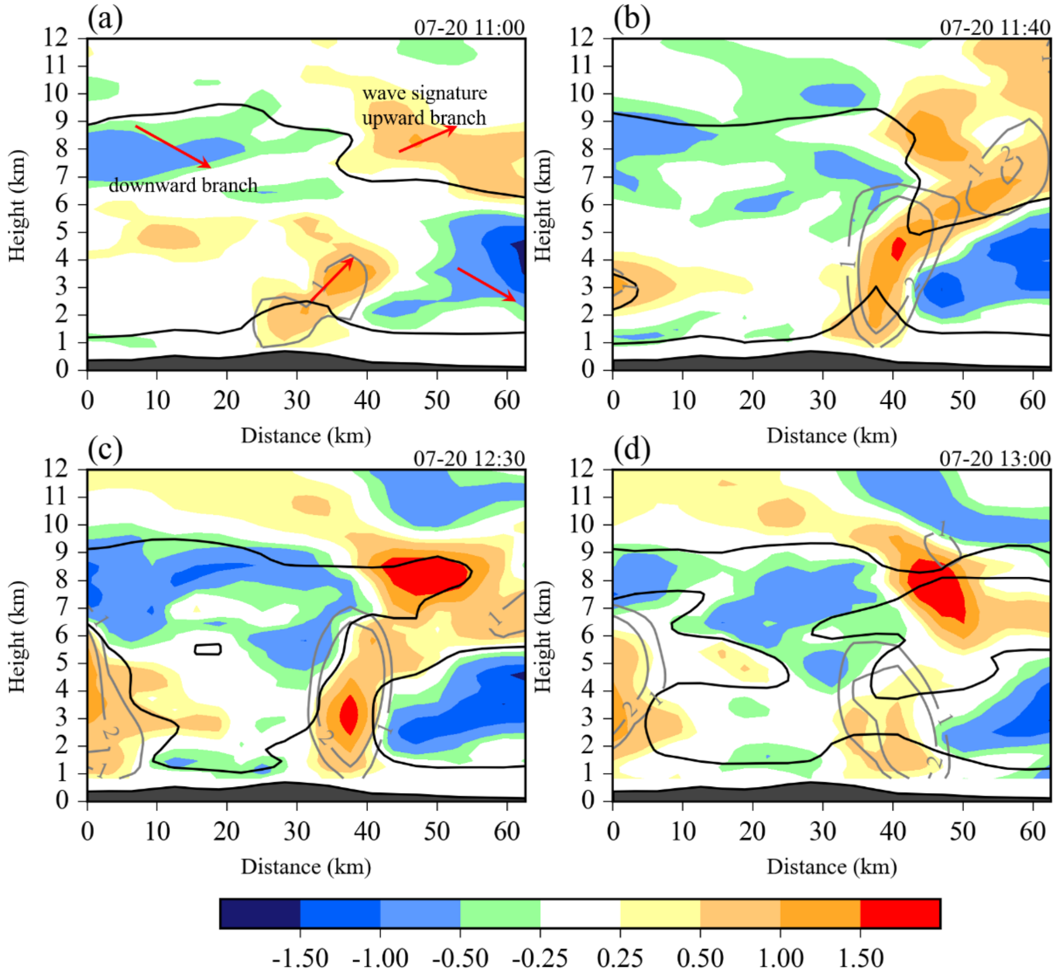

Figure 14. Vertical cross section of gravity wave–related variables in the southwest–northeast direction through the rainfall center. Potential temperature perturbations (K; colors) indicating buoyancy, vertical velocity (m s^{-1}; gray contours), and equivalent potential temperature (350 K, black contours) representing streamlines are shown.The location of the cross section is marked by a black arrow within the blue rectangle in Figure 11b. The time of each panel is (a) 1100, (b) 1140, (c) 1230, (d) 1300 CST on July 20, 2021.

5 Conclusions and discussions

Based upon radar, sounding, precipitation observations, ERA5 reanalysis, and a series of sensitivity simulations, this study investigates the characteristics and mechanisms of gravity waves associated with banded convection between the rainfall center and the southwest mountain (FNM), and effects of these gravity waves on the extreme rainfall. The main conclusions are as follows:

Gravity waves play as a robust factor in “21.7” rainfall event. These gravity waves were excited in the middle layer of the troposphere when the southwesterly flow in front of the MCV located west of the rainfall center impinged on the northwest-southeast trending mountain (FNM). These waves moved northeastward towards the rainfall center and generated banded convection between the center and the southwest mountain. Power spectrum analysis indicates that simulated gravity waves in the banded convective activity feature a wave phase speed of around 11.5 m s^{-1} with wavelengths of 60-90 km and periods of 90-150 minutes.

The gravity wave was excited above the mountain FNM located to southeast of the rainfall center, due to the thermal stability of the atmosphere ($N_m^2 > 0$) and the sudden decrease of the squared score parameter l^2 caused by strong wind shear. The gravity waves exhibit horizontal propagation with a duration of over 6 hours for wave-ducting effects, which allow for horizontal propagation with minimal energy loss. The wave-ducting effects exist between the terrain and the rainfall center, with a ducting stable layer in the middle layer of the troposphere (~7 km altitude), a reflecting layer above 8 km altitude, and a critical layer in the reflecting layer.

Sensitivity experiments with different intensities of gravity waves in the vicinity of the FNM suggest that, the gravity waves lead to an approximately 20% increase in precipitation over the rainfall center. After propagating 60 km northeast, the gravity wave peak subsequently is embedded in the quasi-stationary convective system (QSCS) over the rainfall center, resulting in the downward transportation of wave energy from the upper troposphere. Simultaneously, the low-level gravity waves were excited due to the latent heating dispersion from the QSCS at the lower tropospheric level, leading to an upward dispersion of wave energy. The downward and upward flux of gravity wave energy led to a convergence of wave energy in the middle levels, which transferred wave energy into vertical kinetic energy, ultimately strengthening the convection.

The mechanism of gravity waves activity is summarized as a conceptual model shown in Figure 15.

This study suggests that the orographic gravity wave, associated with conditionally unstable moist airflows produced by westerly trough pass through a small terrain, is an important mesoscale factor contributing to the intensification of the “21.7” event. Similar orographic gravity waves may also contribute to rainfall over other complex terrain areas, such as the coastal range in Western Oregon (Kirshbaum et al., 2007b), Taiwan's Central Mountain Range (Tang et al., 2012), southern China's Coastal Range (Bai et al., 2021), and Helan Mountain (Chen et al., 2021). Future research will examine how and to what extent orographic gravity waves contribute to the extreme rainfall in these areas. Additionally, a detailed investigation of the interactions between gravity waves at high and low tropospheric levels would be an interesting topic worth exploring in future studies.

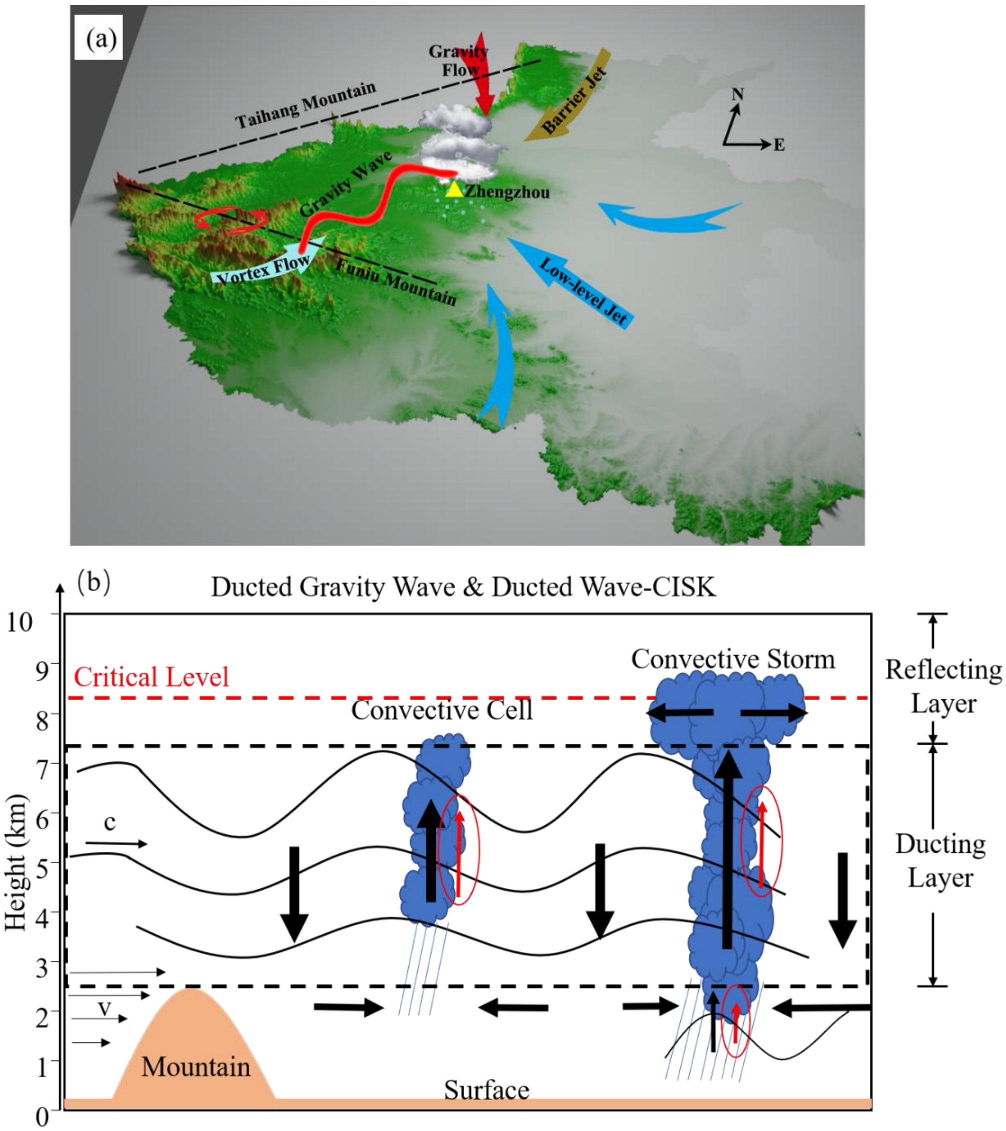

Figure 15. Schematic depiction of gravity wave activity during the "21.7" extreme rainfallevent. (a) Gravity waves and other mesoscale weather system processes, (b) Mechanism of ducted linear gravity wave train propagating and it's couple to deep convection. In Figure15a, the research area is Henan Province, the gold triangle is the location of extreme precipitation (Zhengzhou City). The light blue, blue, brown and red arrows represent the the southwesterly flow from the MCV, low-level jet related to the outflow of typhoon "Infa", barrier jet on the eastern slope of the Taihang Mountain, and the downslope gravity flow originating from the top of the Taihang Mountain. The red circular arrows indicate the midlevel circulation of the meso-low, and the red wavy lines represent the gravity wave (mountain wave).In Figure 15b, the black wavy lines (isentropic lines) represent gravity wave activity, the black arrows represent convergence, divergence, and upward or downward motion induced by gravity wave activity, the dashed line indicate the ducting stable layer covered by a critical level (showed in dashed red lines), and encircled red arrows denote latent heating-induced vertical motion. Modified from Ralph et al. (1993).

Acknowledgments

This work is supported by the National Natural Science Foundation of China (No. 42175064 and 41471034) and the Natural Science Foundation of Gansu Province of China (20JR10RA654). We thank Dr. Li Xin from Nanjing Joint Institute for Atmospheric Sciences (NJIAS) for sharing the automatic observations. We sincerely thank the Supercomputing Center of Lanzhou University for providing the computational resources.

Open Research

The ERA5 hourly data is available at https://doi.org/10.24381/cds.bd0915c6. The model data for this study are available on the website (http://dx.doi.org/10.6084/m9.figshare.24994143).

References

Bai, L., Chen, G., Huang, Y., & Meng, Z. (2021). Convection Initiation at a Coastal Rainfall Hotspot in South China: Synoptic Patterns and Orographic Effects. Journal of Geophysical Research: Atmospheres, 126(24), e2021JD034642. https://doi.org/10.1029/2021JD034642

Beljaars, A. C. M., Brown, A. R., & Wood, N. (2004). A new parametrization of turbulent orographic form drag. Quarterly Journal of the Royal Meteorological Society, 130(599), 1327–1347. https://doi.org/10.1256/qj.03.73

Booker, J. R., & Bretherton, F. P. (1967). The critical layer for internal gravity waves in a shear flow. Journal of Fluid Mechanics, 27(3), 513–539. https://doi.org/10.1017/S0022112067000515

Bosart, L. F., Bracken, W. E., & Seimon, A. (1998). A Study of Cyclone Mesoscale Structure with Emphasis on a Large-Amplitude Inertia–Gravity Wave. Monthly Weather Review, 126(6), 1497–1527. https://doi.org/10.1175/1520-0493(1998)126<1497:ASOCMS>2.0.CO;2

Bryan, G. H., & Fritsch, J. M. (2002). A Benchmark Simulation for Moist Nonhydrostatic Numerical Models. Monthly Weather Review, 130(12), 2917–2928. https://doi.org/10.1175/1520-0493(2002)130<2917:ABSFMN>2.0.CO;2

Buijsman, M. C., Arbic, B. K., Kelly, S. M., & Waterhouse, A. F. (2019). Internal Gravity Waves. In Encyclopedia of Ocean Sciences (pp. 622–632). Elsevier. https://doi.org/10.1016/B978-0-12-409548-9.04160-9

Chen, Y., Su, Y., Yang, Y., Zhang, S., & Yang, J. (2021). The Mesoscale Characteristics of Extreme Rainstorm in the Eastern Region of Helan Mountain. Plateau Meteorology, 40(1), 47–60. https://doi.org/10. 7522/j. issn. 1000-0534. 2020. 00012.

Chu, C., & Lin, Y. (2000). Effects of Orography on the Generation and Propagation of Mesoscale Convective Systems in a Two-Dimensional Conditionally Unstable Flow. Journal of the Atmospheric Sciences, 57(23), 3817–3837. https://doi.org/10.1175/1520-0469(2001)057<3817:EOOOTG>2.0.CO;2

Chyi, D., He, L., Wang, X., & Chen, S. (2022). Fine Observation Characteristics and Thermodynamic Mechanisms of Extreme Heavy Rainfall in Henan on 20 July 2021. Journal of Applied Meteorological Science (in Chinese), 33(1), 1–15. https://doi.org/10.11898/1001-7313.20220101

Ding, Y., Cai, Z., & Li, J. (1978). A case study on the excessively severe rain storm in Henan province, early in August, 1975. Chinese Journal of Atmospheric Sciences (in Chinese), (4), 276–289. https://doi.org/10.3878/j.issn.1006-9895.1978.04.02

Du, Y., & Zhang, F. (2019). Banded Convective Activity Associated With Mesoscale Gravity Waves Over Southern China. Journal of Geophysical Research: Atmospheres, 124(4), 1912–1930. https://doi.org/10.1029/2018JD029523

Durran, D., & Klemp, J. (1982). On the Effects of Moisture on the Brunt-Väisälä Frequency. Journal of The Atmospheric Sciences - J ATMOS SCI, 39, 2152–2158. https://doi.org/10.1175/1520-0469(1982)039<2152:OTEOMO>2.0.CO;2

Fovell, R. G., Mullendore, G. L., & Kim, S.-H. (2006). Discrete Propagation in Numerically Simulated Nocturnal Squall Lines. Monthly Weather Review, 134(12), 3735–3752. https://doi.org/10.1175/MWR3268.1

Fu, S., Zhang, Y., Wang, H., Tang, H., Li, W., & Sun, J.-H. (2022). On the Evolution of a Long-Lived Mesoscale Convective Vortex that Acted as a Crucial Condition for the Extremely Strong Hourly Precipitation in Zhengzhou. Journal of Geophysical Research: Atmospheres, 127(11), e2021JD036233. https://doi.org/10.1029/2021JD036233

Ghanmi, I., Salavec, P., & Barcza, Z. (2020). Application of Scorer-parameter in Mountain Wave Forecasting at the Hungarian Meteorological Service. Eötvös Loránd University.

Hersbach, H., Bell, B., Berrisford, P., Hirahara, S., Horányi, A., Muñoz-Sabater, J., et al. (2020). The ERA5 global reanalysis. Quarterly Journal of the Royal Meteorological Society, 146(730), 1999–2049. https://doi.org/10.1002/qj.3803

Hong, S.-Y., & Lim, J.-O. J. (2006). The WRF single-moment 6-class microphysics scheme (WSM6). Asia-Pacific Journal of Atmospheric Sciences, 42(2), 129–151.

Hong, S.-Y., Noh, Y., & Dudhia, J. (2006). A New Vertical Diffusion Package with an Explicit Treatment of Entrainment Processes. Monthly Weather Review - MON WEATHER REV, 134. https://doi.org/10.1175/MWR3199.1

Hua, S., Xu, X., & Chen, B. (2020). Influence of Multiscale Orography on the Initiation and Maintenance of a Precipitating Convective System in North China: A Case Study. Journal of Geophysical Research: Atmospheres, 125(13), e2019JD031731. https://doi.org/10.1029/2019JD031731

Huang, D. (2022). The atmospheric structure and dual-polarization radar echoes analysis of the “21·7” Henan Province extremely heavy rainfall (Master). Nanjing University of Information Science & Technology. https://doi.org/10.27248/d.cnki.gnjqc.2022.000115.

Iacono, M. J., Delamere, J. S., Mlawer, E. J., Shephard, M. W., Clough, S. A., & Collins, W. D. (2008). Radiative forcing by long-lived greenhouse gases: Calculations with the AER radiative transfer models. Journal of Geophysical Research: Atmospheres, 113(D13). https://doi.org/10.1029/2008JD009944

Kain, J. S. (2004). The Kain–Fritsch Convective Parameterization: An Update. Journal of Applied Meteorology and Climatology, 43(1), 170–181. https://doi.org/10.1175/1520-0450(2004)043<0170:TKCPAU>2.0.CO;2

Kim, Y., & Doyle, J. D. (2005). Extension of an orographic-drag parametrization scheme to incorporate orographic anisotropy and flow blocking. Quarterly Journal of the Royal Meteorological Society, 131(609), 1893–1921. https://doi.org/10.1256/qj.04.160

Kim, Y.-J., & Arakawa, A. (1995). Improvement of Orographic Gravity Wave Parameterization Using a Mesoscale Gravity Wave Model. Journal of the Atmospheric Sciences, 52(11), 1875–1902. https://doi.org/10.1175/1520-0469(1995)052<1875:IOOGWP>2.0.CO;2

Kingsmill, D. E., Persson, P. O. G., Haimov, S., & Shupe, M. D. (2016). Mountain waves and orographic precipitation in a northern Colorado winter storm. Quarterly Journal of the Royal Meteorological Society, 142(695), 836–853. https://doi.org/10.1002/qj.2685

Kirshbaum, D. J., Rotunno, R., & Bryan, G. H. (2007). The Spacing of Orographic Rainbands Triggered by Small-Scale Topography. Journal of the Atmospheric Sciences, 64(12), 4222–4245. https://doi.org/10.1175/2007JAS2335.1

Kruse, C. G., & Smith, R. B. (2015). Gravity Wave Diagnostics and Characteristics in Mesoscale Fields. Journal of the Atmospheric Sciences, 72(11), 4372–4392. https://doi.org/10.1175/JAS-D-15-0079.1

Kusunoki, K., Eito, H., & Akaeda, K. (2000). A Case Study of Low-level Internal Gravity Waves using Doppler Radar and ACARS. Journal of the Meteorological Society of Japan. Ser. II, 78(5), 511–525. https://doi.org/10.2151/jmsj1965.78.5_511

Liang, X., Xia, R., Bao, X., Zhang, X., Wang, X., Su, A., et al. (2022). Preliminary investigation on the extreme rainfall event during July2021 in Henan Province and its multi-scale processes. Chinese Science Bulletin (in Chinese), 67(10), 997–1011. https://doi.org/10.1360/TB-2021-0827

Lindzen, R. S., & Tung, K.-K. (1976). Banded Convective Activity and Ducted Gravity Waves. Monthly Weather Review, 104(12), 1602–1617. https://doi.org/10.1175/1520-0493(1976)104<1602:BCAADG>2.0.CO;2

Lindzen, Richard S. (1974). Wave-CISK in the Tropics. Journal of the Atmospheric Sciences, 31(1), 156–179. https://doi.org/10.1175/1520-0469(1974)031<0156:WCITT>2.0.CO;2

Luo, Y., & Du, Y. (2022). The Roles of Low-level Jets in "21·7" Henan Extremely Persistent Heavy Rainfall Event. ADVANCES IN ATMOSPHERIC SCIENCES. https://doi.org/10.1007/s00376-022-2026-1

Nappo, C. J. (2013). An introduction to atmospheric gravity waves (2nd ed). Waltham, MA: Elsevier.

Ralph, F. M., Venkateswaran, V., & Crochet, M. (1993). Observations of a Mesoscale Ducted Gravity Wave. Journal of the Atmospheric Sciences, 50(19), 3277–3291. https://doi.org/10.1175/1520-0469(1993)050<3277:OOAMDG>2.0.CO;2

Ran, L., Li, S., Zhou, Y., Yang, S., Ma, S., Zhou, K., et al. (2021). Observational Analysis of the Dynamic, Thermal, and Water Vapor Characteristics of the "7.20" Extreme Rainstorm

Event in Henan Province, 2021. Chinese Journal of Atmospheric Sciences (in Chinese), 45(06), 1366–1383. https://doi.org/10.3878/j.issn.1006-9895.2109.21160

Raymond, D. J. (1975). A Model for Predicting the Movement of Continuously Propagating Convective Storms. Journal of the Atmospheric Sciences, 32(7), 1308–1317. https://doi.org/10.1175/1520-0469(1975)032<1308:AMFPTM>2.0.CO;2

Schumacher, R. S. (2009). Mechanisms for Quasi-Stationary Behavior in Simulated Heavy-Rain-Producing Convective Systems. Journal of the Atmospheric Sciences, 66(6), 1543–1568. https://doi.org/10.1175/2008JAS2856.1

Schumacher, R. S., & Johnson, R. H. (2005). Organization and Environmental Properties of Extreme-Rain-Producing Mesoscale Convective Systems. Monthly Weather Review, 133(4), 961–976. https://doi.org/10.1175/MWR2899.1

Schumacher, R. S., & Rasmussen, K. L. (2020). The formation, character and changing nature of mesoscale convective systems. Nature Reviews Earth & Environment, 1(6), 300–314. https://doi.org/10.1038/s43017-020-0057-7

Scorer, R. S. (1949). Theory of waves in the lee of mountains. Quarterly Journal of the Royal Meteorological Society, 75(323), 41–56. https://doi.org/10.1002/qj.49707532308

Skamarock, C., Klemp, B., Dudhia, J., Gill, O., Liu, Z., Berner, J., et al. (2021). A Description of the Advanced Research WRF Model Version 4.3. https://doi.org/10.5065/1dfh-6p97

Steeneveld, G. J., Holtslag, A. a. M., Nappo, C. J., Wiel, B. J. H. van de, & Mahrt, L. (2008). Exploring the Possible Role of Small-Scale Terrain Drag on Stable Boundary Layers over Land. Journal of Applied Meteorology and Climatology, 47(10), 2518–2530. https://doi.org/10.1175/2008JAMC1816.1

Su, A., LÜ, X., Cui, L., Li, Z., Xi, L., & Li, H. (2021). The Basic Observational Analysis of “7.20” Extreme Rainstorm in Zhengzhou. Torrential Rain and Disasters (in Chinese), 40(5), 445–454. https://doi.org/10.3969/j.issn.1004-9045.2021.05.001

Sun, J., Li, R., Zhang, Q., Trier, S. B., Ying, Z., & Xu, J. (2023). Mesoscale factors contributing to the extreme rainstorm on 20 July 2021 in Zhengzhou, China as revealed by rapid update 4DVar analysis. Monthly Weather Review, 1(aop). https://doi.org/10.1175/MWR-D-22-0337.1

Sun, S., Shi, C., Pan, Y., Bai, L., Xu, B., Zhang, T., et al. (2020). Applicability Assessment of the 1998–2018 CLDAS Multi-Source Precipitation Fusion Dataset over China. Journal of Meteorological Research, 34(4), 879–892. https://doi.org/10.1007/s13351-020-9101-2

Tang, X.-D., Yang, M.-J., & Tan, Z.-M. (2012). A modeling study of orographic convection and mountain waves in the landfalling typhoon Nari (2001). Quarterly Journal of the Royal Meteorological Society, 138(663), 419–438. https://doi.org/10.1002/qj.933

Tao, S. (1980). Heavy Rainfalls in China. Beijing: Science Press (in Chinese).

Wang, C., Wu, D., & Zhang, F. (2019). Modification of the convective adjustment time-scale in the Kain–Fritsch eta scheme for the case of weakly forced deep convection over the Tibetan Plateau region. Quarterly Journal of the Royal Meteorological Society, 145(722), 1915–1932. https://doi.org/10.1002/qj.3535

Wei, P., Xu, X., Xue, M., Zhang, C., Wang, Y., Zhao, K., et al. (2023). On the Key Dynamical Processes Supporting the 21.7 Zhengzhou Record-breaking Hourly Rainfall in China. Advances in Atmospheric Sciences, 40(3), 337–349. https://doi.org/10.1007/s00376-022-2061-y

Wheeler, M., & Kiladis, G. N. (1999). Convectively Coupled Equatorial Waves: Analysis of Clouds and Temperature in the Wavenumber–Frequency Domain. Journal of the Atmospheric Sciences, 56(3), 374–399. https://doi.org/10.1175/1520-0469(1999)056<0374:CCEWAO>2.0.CO;2

Wu, D., Wang, C., & He, G. (2016). Gravity Wave Characteristics in Two Summer Heavy Rainfall in the Qinghai-Xizang Plateau. Plateau Meteorology (in Chinese), 854–864. https://doi.org/10.7522/j.issn.1000-0534.2015.00066

Xu, X., Li, R., Teixeira, M. A. C., & Lu, Y. (2021). On the Momentum Flux of Vertically-Propagating Orographic Gravity Waves Excited in Nonhydrostatic Flow over Three-dimensional Orography. Journal of the Atmospheric Sciences. https://doi.org/10.1175/JAS-D-20-0370.1

Yang, M.-J., & Houze, R. A. (1995). Multicell Squall-Line Structure as a Manifestation of Vertically Trapped Gravity Waves. Monthly Weather Review, 123(3), 641–661. https://doi.org/10.1175/1520-0493(1995)123<0641:MSLSAA>2.0.CO;2

Zhang, F., Davis, C. A., Kaplan, M. L., & Koch, S. E. (2001). Wavelet analysis and the governing dynamics of a large-amplitude mesoscale gravity-wave event along the East Coast of the United States. Quarterly Journal of the Royal Meteorological Society, 127(577), 2209–2245. https://doi.org/10.1002/qj.49712757702